Chapter 5

Hysteric photo-conduction and negative differential resistance in cesium lead bromide

Publication: ***Manish Kumar****, Priyanka A. Jha, Pardeep K. Jha, and Prabhakar Singh, J. Appl. Phys. 127, 224904 (2020).*

CHAPTER 5: Hysteric Photo-Conduction and Negative Differential Resistance in Cesium Lead Bromide

5.1 Introduction

It has already been discussed in chapter 4, all inorganic ($CsPbI_3$ and $CsPbBr_3$) perovskite halides are stable intrinsically as suggested by their thermal analysis. However, the $CsPbBr_3$ sample is more stable than that of $CsPbI_3$. Moreover, the Cesium lead bromide sample shows the highest value of current as compared to the other synthesized inorganic materials in the continuous exposure of AM 1.5G sunlight. Nevertheless, the extrinsic factors such as heat, moisture, electric field, etc., do not allow $CH_3NH_3PbI_3$ to last long; however, all-inorganic perovskite is quite stable (structurally) in their bulk form, although the stability of perovskite halides under light (photo-stability) is also a big issue that has not been probed extensively [140],[75],[177]. Furthermore, as we understand that photo-instability of perovskite halides is in correlation with the problem of current-voltage hysteresis, which needs to be addressed to estimate the true photon to electron efficiency. However, to address the issue of hysteresis, there are a few points, viz., (i) the time scale required for the redistribution of the mobile ions, (ii) the interaction between ion migration and electrode polarization, (iii) how the interfacial photo-electrons/ holes with trapped charges and mobile ions create an impact on the capacitive current, and (iv) band bending, that are required to be investigated. It is also the subject of current research that how the traps originate from immobile defects (defect proliferation) or ion migration and how these traps affect non-steady current.

To investigate these issues, we have prepared the polycrystalline bulk sample of $CsPbBr_3$ by the cold sintering (CS)–solid-state reaction (SSR) route, which is found to be stable thermally and structurally in an ambient environment with a Pnma crystal structure at room temperature. Earlier scientific community has studied the hysteresis for PSCs; however, in order to find out whether the hysteresis is an intrinsic property of the active material, we are studying the stable form of $CsPbBr_3$ as the external factors leading to photo-instability will vanish. In this chapter, we illuminate the $CsPbBr_3$ sample with AM 1.5 G Sun light longitudinally for 3 h and studied the conduction mechanism [forward scan (FS) as well as reverse scan (RS)] at regular intervals of time after illumination along with dark. We observe higher Coulomb screening and negative differential resistance in the FS, which is related to carrier enhancement at localized sites. This study will further lead the scientific community to investigate whether this drift velocity slow- down is related to the Gunn effect or the Rashba effect.

5.2 Experimental procedure

The polycrystalline bulk sample of $CsPbBr_3$ was synthesized by Cold sintering (CS)–Solid state reaction (SSR) route. For preparing $CsPbBr_3$, the powders of CsBr (99.999%, Aldrich) and $PbBr_2$ (98%, Aldrich) were weighed in stoichiometric quantities. The details of synthesis process has already been explained in the previous chapter.

The ultraviolet–visible (UV–VIS) absorption and the photoluminescence spectrum of the powder sample are measured by a JASCO V-770 ultraviolet–visible (UV–VIS) spectrometer and a 450 W Illuminator model FL-1039A/40 A spectrometer, respectively. For electrical measurements, contacts were made using room temperature Ag paste. The impedance measurements were done using a Wayne Kerr 6500 LCR meter from RT to 150 °C in the frequency range of 20 Hz to 1 MHz. The current–voltage (I–V) measurement is performed using a Keithley 2450 source meter on exposure to radiation through a Sciencetech solar simulator class: AA with AM 1.5 G and a higher collimated beam in a longitudinal mode at a fixed scan rate (variation of hysteresis with different scan rates minimum hysteresis is observed at 1.66 V/s) of 1.66 V/s in a dual sweep mode from 10 V to -10 V (Fig. 5.1). The I–V hysteresis of $CsPbBr_3$ is taken in dark and room light and with continuous illumination of AM 1.5 G Sun light (at a few intervals of time, 0 h, 0.5 h, 1.0 h, 1.5 h, 2.0 h, and 3.0 h). All measurements are done in an ambient environment.

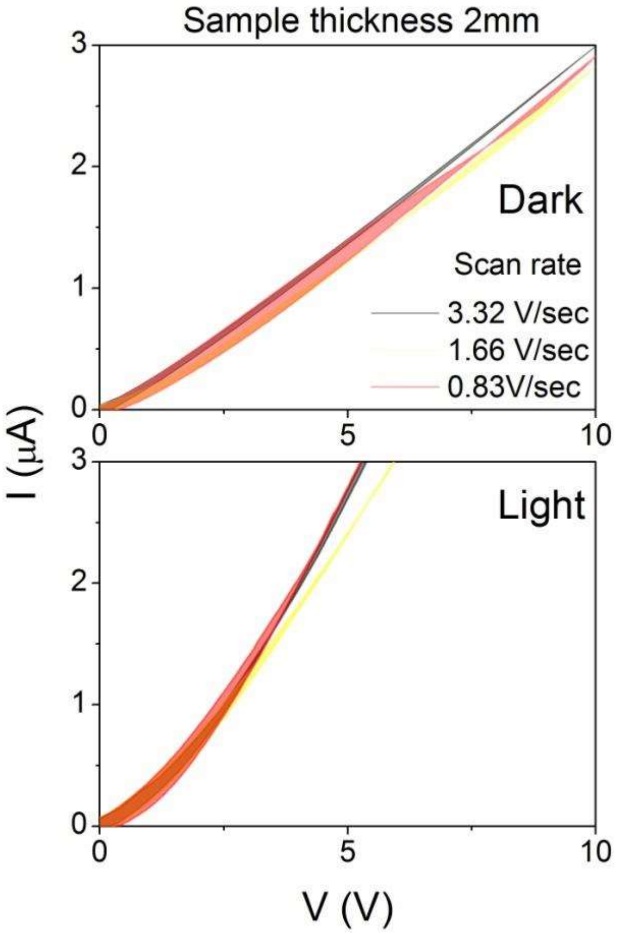

Figure 5.1: I-V characteristics with the different scan rates of $CsPbBr_3$ synthesized via Cold sintering technique (6-month-old sample).

5.3 Results and Analysis

5.3.1 Observation of I-V hysteresis

We are presenting the hysteresis (I–V curve) of $CsPbBr_3$ measured at the illumination of AM 1.5 G Sun light [see Fig. 5.2(c)] at different time intervals indicated by arrows marks on the light intensity vs the time plot [the bottom right inset of Fig. 5.2(c)]. Figure 5.2(d) shows variation in the hysteresis area with the voltage in dark and room light (RL).

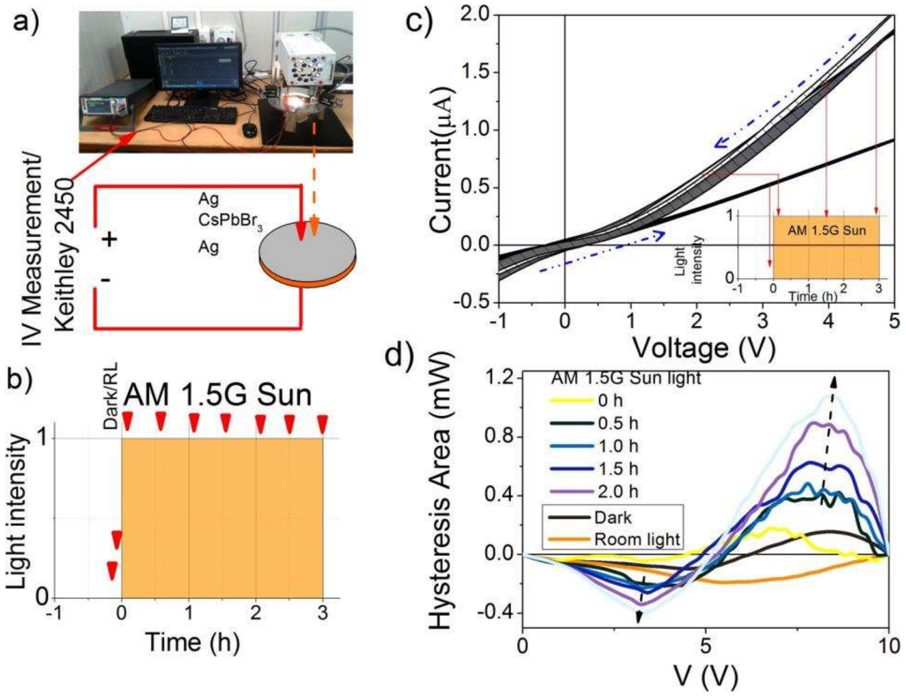

Figure 5.2: (a) Experimental setup for I–V measurements showing the light and sample alignment in air (not in an inert atmosphere). (b) Time scale for the measurement of I–V characteristics. Just after dark and room light measurements, solar simulator was switched on and then continuously, the sample was illuminated for 3 h. (c) Observation of I–V hysteresis in $CsPbBr_3$ with an illumination of AM 1.5 G Sun light taken at time intervals as line marked with an arrow on the light intensity and the time plot (right bottom corner). On the time scale, the origin is the start of illumination of the Sun light on the sample surface and (d) shows variation in the hysteresis area with the voltage in dark, room light (RL) and with a continuous illumination of AM 1.5 G Sun light (at a few intervals of time, 0 h, 0.5 h, 1.0 h, 1.5 h, 2.0 h, and 3.0 h).

For insight understanding of the I–V characteristics, we have studied the forward scan (FS) and the reverse scan (RS) in detail and replaced the current by the current density, J (surface area, A = 100 mm^2), and the voltage by the electric field, E (distance between the electrode, d = 1 mm). The FS and RS curves are fitted with $J = kE^n$, where n is the parameter that measures the deviation from Ohm's law and k is the proportionality constant, which can be correlated with the charge density and mobility. Figure 5.3 (a) shows the variation of these parameters "n" and "k" with the (AM 1.5 G Sun light) illumination time for both forward scan (FS) and reverse scan (RS) with the fitted curves in the inset. It is observed that for both FS and RS, the value of the exponent "n" >1 for dark current and is increasing almost exponentially with illumination time. However, there is a significant variation in the proportionality factor "k." With the illumination, k is observed to increase suddenly, and thereafter, it decreases up to 90 min with a further small exponential rise. Analogically to the Drude relation $J = (ne\mu) E$ (and hence Ohm's law; i.e., $J = \sigma E$; the simple case with n = 1 and $k = \sigma$), "k" in relation to $J = kE^n$ can be correlated with the conductivity "σ" in relation to $J = \sigma E$; therefore, σ–E curves are plotted for FS and RS [Fig. 5.3 (b)]. The difference in the behavior of FS and RS is clearly visible here. We have divided σ–E curves in the two field regime for both scans. For FS, (i) the low field regime (E < 1 kV/m) where conductivity decreases to a minimum value and (ii) the mid-field regime where there is a two slope rise (a) midfield regime I (1 kV/m < E < 4 kV/m) with a faster rise in conductivity and (b) mid-field regime II (up to E > 4 kV/m) with a slower rise in conductivity. While for RS, σ–E curves can be divided in the two field regime as (i) the low field regime (E < 1 kV/m) where conductivity increases sharply, thereafter slower (almost saturating) rise and (ii) the mid-field regime (up to E > 1 kV/m). However, in a low field, the ohmic contact dominates; therefore, "n" should approach to 1. To understand the conduction behavior, the electric potential must overcome the thermal fluctuations; thus, we are not considering the feature in a low field regime. At room temperature in a mid- field regime (V > 1 V), potential is sufficiently enough to overcome the thermal fluctuations; i.e., $q\beta V > 38$ (here, q is the charge on the carriers and β is the Boltzmann factor). In order to study the comparative conduction behavior in the mid-field regime, we (propose to) fit the σ–*E* curves with the modified Arrhenius relation by inclusion of constants on account of photo-current and the deviation from the Drude relation (σ_p and k_1, respectively) as per the relation

$$\sigma = \sigma_p + \sigma_0\, e^{(k_1 q\beta d)\,E} \tag{5.1}$$

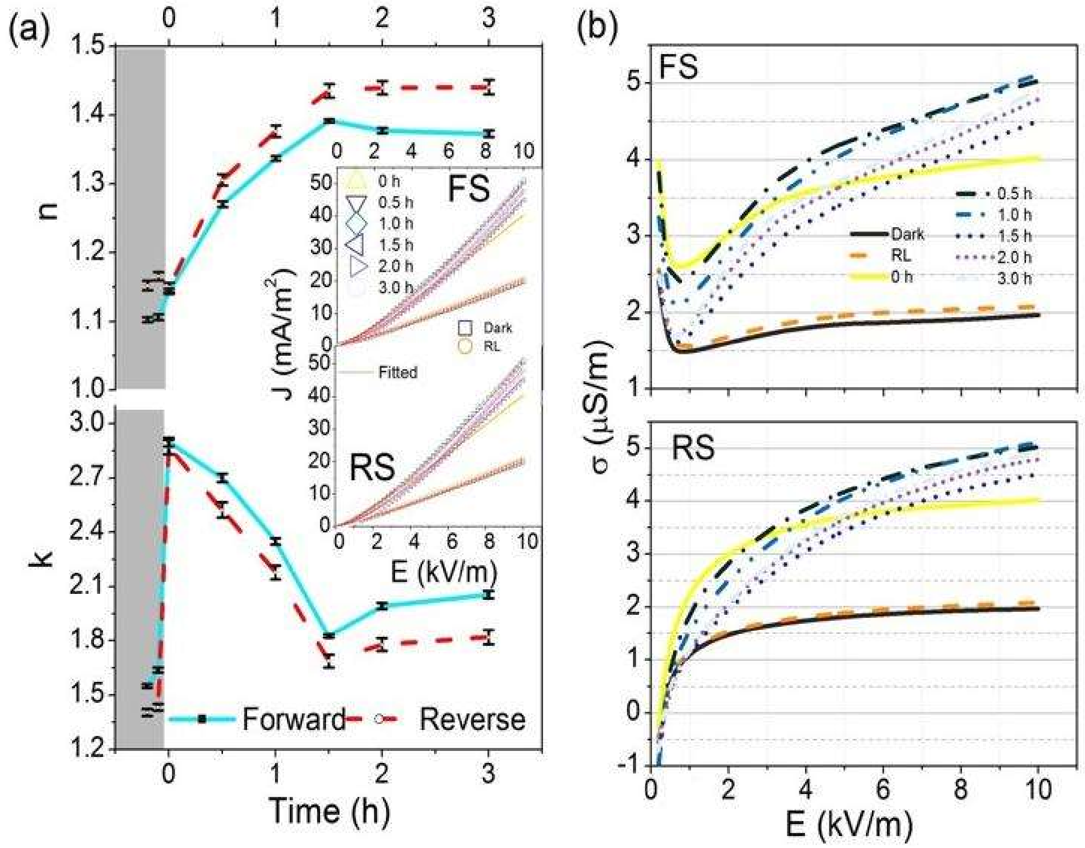

Figure 5.3: (a) Variation of extracted parameters “n” and “k” (lines are to guide only) from fitting $J = kE^n$ for both forward scan (FS) and reverse scan (RS) shown in the inset and (b) the variation of conductivity with an electric field for $CsPbBr_3$ in dark, room light (RL) and with a continuous illumination of AM 1.5 G Sun light (at a few intervals of time, 0 h, 0.5 h, 1.0 h, 1.5 h, 2.0 h, and 3.0 h).

The σ–*E* curves obtained [Fig. 5.3 (b)] are fitted using the relation (5.1) for both FS and RS. For clarity, Fig. 5.4 (a) shows the fitting for dark conductivity and just illuminated (t = 0 h) photoconductivity only. The parameters (σ_p, σ_0, and $E_0 = 1/k_1 q\beta d$, respectively), are extracted, and their variation with illumination time is plotted in Figs. 5.4 (b) – 5.4 (d). It is observed that the term σ_p increases significantly (almost double) as soon as the surface is illuminated with AM 1.5 G Sun light, and in the next half an hour, it stabilizes [see Fig. 5.4 (b)]. Furthermore, there is no appreciable difference for FS and RS observed from almost coinciding exponential fitting of the FS and RS variations. However, the later term in Eq. (5.1) has a temperature- field independent parameter σ_0 and a temperature dependent parameter E_0, and both are observed to decrease exponentially with a significant variation for FS and RS [see Figs. 5.4 (c) and 5.4 (d), respectively]. Here, we have two interesting phenomena: (i) σ_0 is negative and (ii) E_0 appears unaffected immediately with photo injection, as observed for the two scans. However, E_0 decreases with illumination time. Until now, we have observed that the dark (or even room light) current–voltage curve does not show significant hysteresis at 300 K even with the field application. However, with the implication of AM 1.5 G spectra, which has a significant contribution in the energy range of 0.5–3 eV with a maximum around 2.3 eV, the hysteresis is observed. Furthermore, the hysteresis increases with an increase in the illumination time. In order to understand we have divided the AM 1.5 G spectra energy into two categories for the given material, (i) $h\nu > E_g$, which is responsible for the photo excitation (say photo-radiation) and (ii) $h\nu \leq E_g$, which is responsible for thermal excitation (say thermal radiation). With the continuous exposure of thermal radiation, the energy may be absorbed and result in the thermionic-field emission.

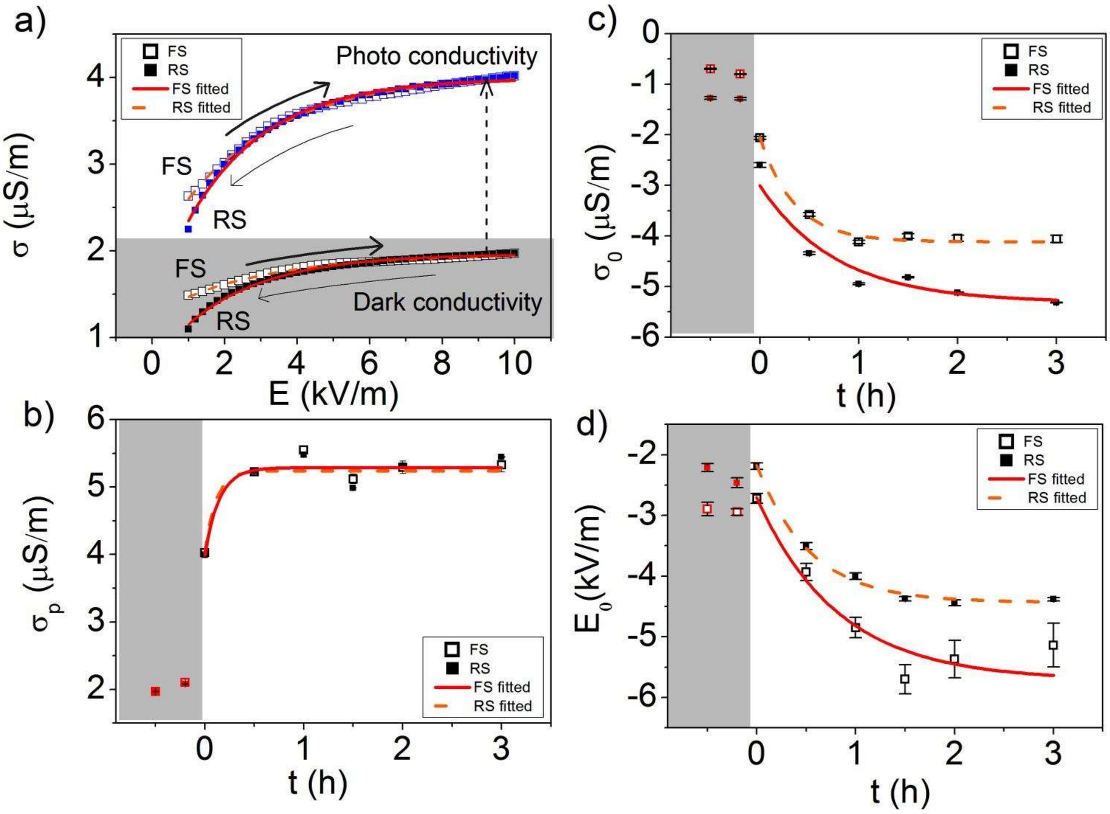

Figure 5.4: (a) The σ–E curves for dark and just illuminated (b)–(d) variation of σ_p, σ_0, and E_0 parameters with illumination time. The negative time scale represents dark current and room light current.

5.3.2 Photo-conduction

In order to understand the mechanism of photo-conduction, we studied time dependent variation of discharge current (after triggering by 5V pulse) with bias voltages of 0 V, 2 V, and 5 V, in dark and AM 1.5 G Sun light illumination for 50 s alternatively (see Fig. 5.5). We observed that the photo generated current increases linearly with the biasing electric field (see the inset of Fig. 5.5). The bandgap energy and Urbach energy are estimated to be ~2.26 eV and ~50 meV, respectively [72].

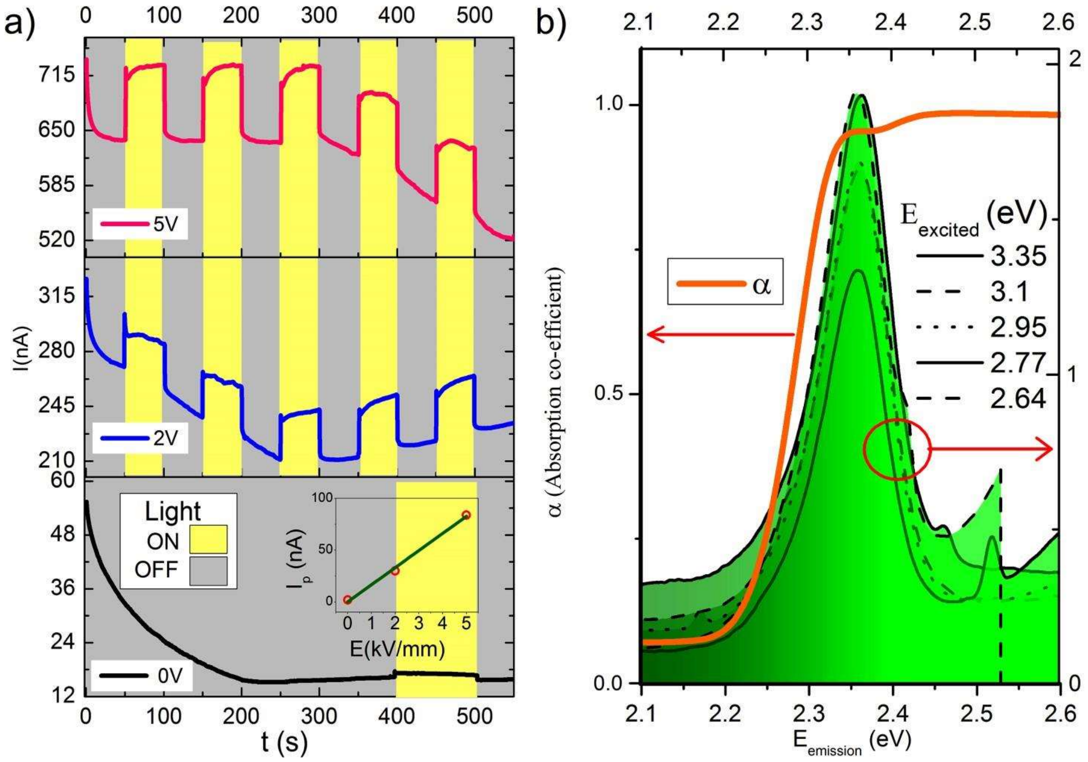

Figure 5.5: (a) With the bias electric field (from the bottom to top: 0 V, 2 V, and 5 V), the photo generated current in a discharge mode after triggering by a 5 V pulse for 50 s. The inset shows a linear variation of the photo generated current with the electric field. (b) Absorption co-efficient and photoluminescence emission spectra with different excitation energies.

However, the room temperature excitonic binding energy extracted from the optical absorption curve [Fig. 5.5 (b)] is estimated to be ~170 meV (2.43-2.26 eV). Also, the luminescence Stoke shift is found to be ~80 meV (2.43–2.35 eV) [Fig. 5.5 (b)] hinting the polaron feature [178].This indicates the exciton generated polaronic conduction. Polaronic conduction usually happens due to hopping of charge carriers in between localized sites. The localized sites in the energy-momentum space here are unlocalized in a real space i.e. hopping of charge carriers in between localized sites. These localized sites act as charged traps sometimes on interactions with excitons due to continuous exposure of photons with hν < Eg. The neutral as well as charged traps can move via hopping with the thermal excitation; however, only charged traps can move (in particular, direction) with the application of fields.

We can estimate the nature of charge carriers by calculating the transport number whether it is ionic, electronic, or mixed. The transport number (~0.72) indicates the type II ionic conductivity in $CsPbBr_3$ [179]. Thus, ion migration cannot be ignored.

5.3.3 Ion dynamics

We have observed that $CsPbBr_3$ possesses ionic as well as electronic charges. To identify the charge species and their dynamics, we fitted the ac conductivity with the Jonscher power law [171] (i.e., $\sigma = \sigma_{dc} + \left(\frac{\sigma_{dc}}{\upsilon_h^{p}}\right) \nu^{p}$, where σ, σ_{dc}, ν, ν_h, and p are conductivity, dc conductivity, frequency, hopping frequency, and exponent, respectively) in the temperature range of 301 K–421 K. In the frequency window 10–106 Hz, the conductivity data could be fitted with the Jonscher power law, in two regimes: (i) the low frequency regime up to 1 kHz (say I) in the temperature range of 351–421 K and (ii) the high frequency regime (10^3 Hz $\leq \nu \leq 10^6$ Hz, say II) in the temperature range of 301–421 K [see Fig. 5.6 (a)]. Generally, for a polycrystalline sample the electrode effect is not observed in the frequency range studied in the present work, thus we guess, the grain boundary (gb) contributes to regime I and the grain (g) contributes to regime II. The dc conductivity, hopping frequency, and exponent are extracted for two regimes, and it is observed that the grain boundary is more resistive than the grain. Also, the Arrhenius plots [$\sigma_{dc} = \sigma_o \exp(-E_a/kBT)$] [Fig. 5.6 (b)] suggest that the grain boundary needs more energy for thermal excitation than the grain. Furthermore, Fig. 5.6 (c) shows a slight superlinear correlation between the hopping frequency and the dc conductivity on a log–log scale (for the grain); however, due to more scattered data points for the grain boundary (not shown), we are unable to conclude. It suggests that with the thermal excitation, there should be an increase in the number of charge species as well as there should be dominant involvement of lighter charge particles. To confirm this, we apply the Ghosh scaling [$\sigma(\nu)/\sigma_{dc} = F(\nu/\nu_h)$] [180] by taking σ_{dc} and ν_h as the scaling parameters in the two regimes.

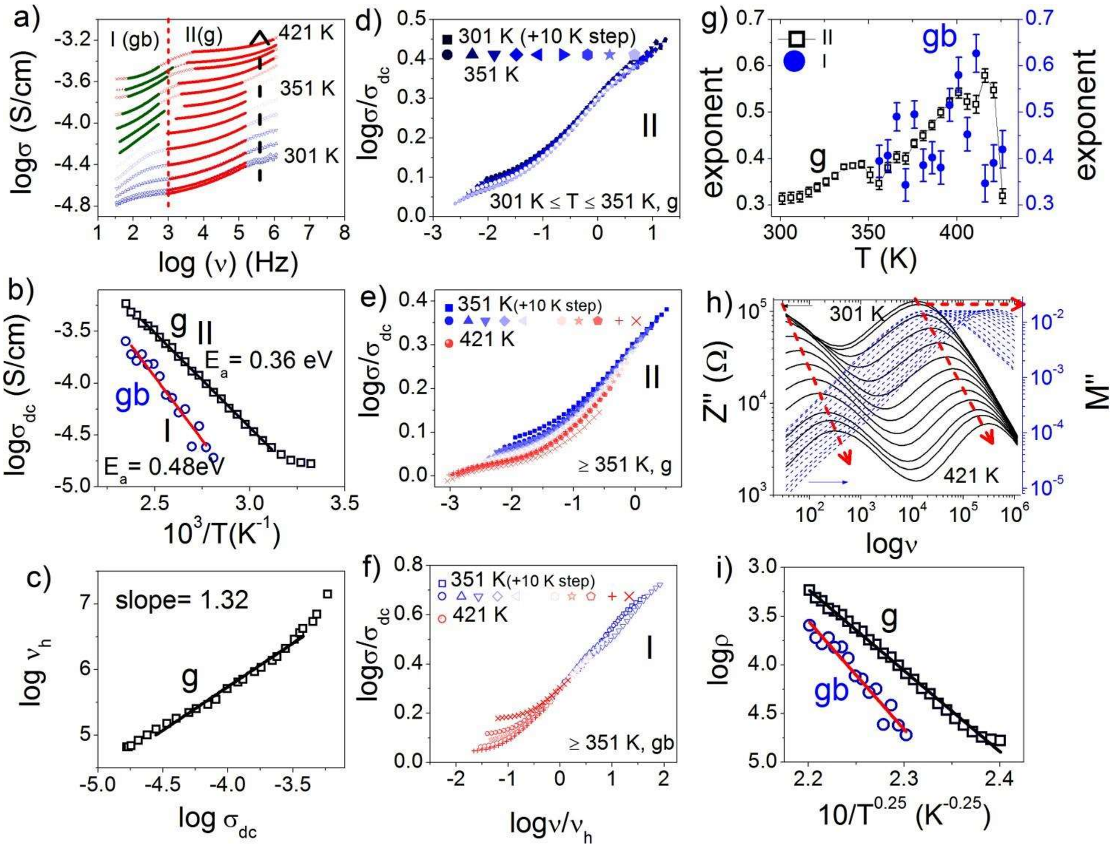

Figure 5.6: (a) Jonscher power fitting log–log σ (conductivity)–ν (frequency) isotherms for the temperature range 301–421 K in regimes I (low frequency regime) and II (high frequency regime). (b) Arrhenius plot of dc conductivity extracted, for regimes I and II. (c) Log– log σ_{dc} (dc conductivity)–ν_h (hopping frequency) plots. (d)–(f) Ghosh scaling for regime II in the temperature range 301–421 K, regime II in the temperature range 351–421 K and regime I in the temperature range 351–421 K. (g) Temperature variation of exponent extracted from the Jonscher fitting. (h) Imaginary impedance and the modulus bode plot and (i) Mott plots for two regimes I and II.

However, as predicted, in regime II [Figs. 5.6 (d) and 5.6 (e)], the deviation from the Ghosh scaling significantly increases at a higher temperature, and Ghosh scaling could not be achieved in regime I. To predict the nature of hopping conduction, the temperature dependent behavior of exponent is explored for the grain as well as the grain boundary [Fig. 5.6 (g)], suggesting a disordered system with small polaron hopping, and this fact is further supported by the difference in the relaxation peak frequency of impedance and the modulus bode plot [Fig. 5.6 (h)]. Furthermore, the resistivity variation can be fitted to the Mott plot using the Mott 3D conduction relation $\rho = \rho_0 \exp (T_0/T)^{1/4}$ [Fig. 5.6 (i)], and the characteristic temperature (T_0) [181] for the grain and the grain boundary is estimated to be ~15 287 K and ~4787 K, respectively. We do not expect any significant variation in the localization length at the grain and the grain boundary; thus, we estimate that the density of localized sites at the Fermi level (α $1/T_0$), is nearly three times for the grain as compared to the grain boundary.

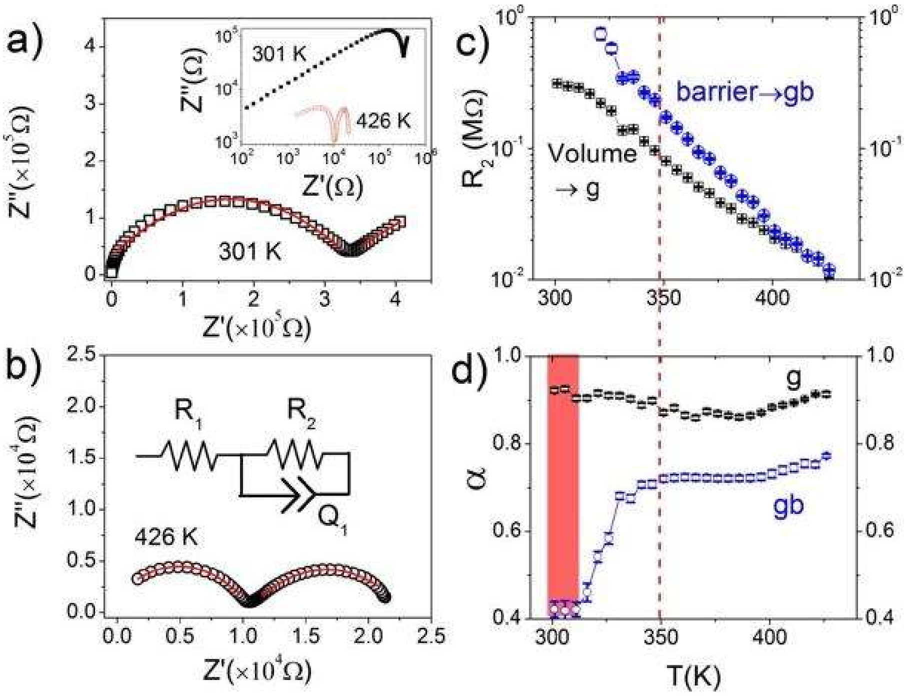

Figure 5.7: (a) Fitted impedance Nyquist plot at 301 K (inset) comparative impedance Nyquist plots on a log scale at temperatures 301 K and 426 K. (b) Fitted impedance Nyquist plot at 426 K with an equivalent circuit in the inset. (c) Variation of the circuit element with the parallel resistance R2 and (d) α, exponent of the constant phase element Q1 for the volume (grain, g) barrier (grain boundary, gb).

Until now, it is confirmed that the grain boundary is more resistive than the grain, and now it is required to understand temperature dependent variation of properties of the grain and the grain boundary. For this, the impedance Nyquist plots are fitted to get an equivalent circuit using Z-view software [Figs. 5.7(a) and 5.7(b)]. We have found a similar equivalent circuit [the inset of Fig. 5.7(b)] for both the low frequency (grain boundary) and the high frequency (grain) arc. The series resistance element, R_1, varies with the temperature dependent structural variation. With the temperature dependent variation of the parallel resistance element, R_2, and the exponent of the constant phase element (Q_1), α is plotted [Figs. 5.7(c) and 5.7(d)].

It is observed that the grain boundary is passive as well as almost diffusive [the temperature regime vertically stripped in Fig. 5.7(d)] in the vicinity of room temperature; however, with a slight increase in the temperature, the grain boundary resistance decreases sharply. Thereafter, both grain and grain boundary resistances decrease but with the capacitive dominant behavior for the grain boundary. For the grain, capacitive behavior is not observed to vary with the temperature. For the temperature $T > 351$ K, the grain boundary resistive behavior approaches to grain behavior, but the kinetics of charge carriers will never be the same, perhaps due to grain–grain boundary interface roughness [182]. In fact, ion dynamics of the present $CsPbBr_3$ sample confirms the Mott type variable range hopping. It is estimated that the density of localized sites at the grain is more than the grain boundary. The activation energy at the grain boundary is ~0.48 eV, which corresponds to Br^- migration, whereas in the grain, the activation energy (~0.3 eV) suggests that ion migration is due to the interstitial movement of Pb^{+2} [96]. Thus, it appears that Pb^{+2} acts as a donor center and becomes the mobile hole generation center. However, ion migration appears to be hindered at the grain boundary due to non-ferroelectric (Br^- - Pb^{+2} – Br^-) dipolar polarization and may be one of the reasons of the slow capacitive behavior observed by many researchers (and references therein).

5.3.4 Thermionic emission

Coming back to observation of σ_0 decreasing with illumination time [Fig. 5.4(c)], this suggests inelastic tunneling of charge carriers due to the interaction of a low energy photon ($h\nu \leq E_g$) with the defect forming electric dipole. It will result in carrier enhancement at localized sites with a consequent decrease in the momentum of hot charge carriers.

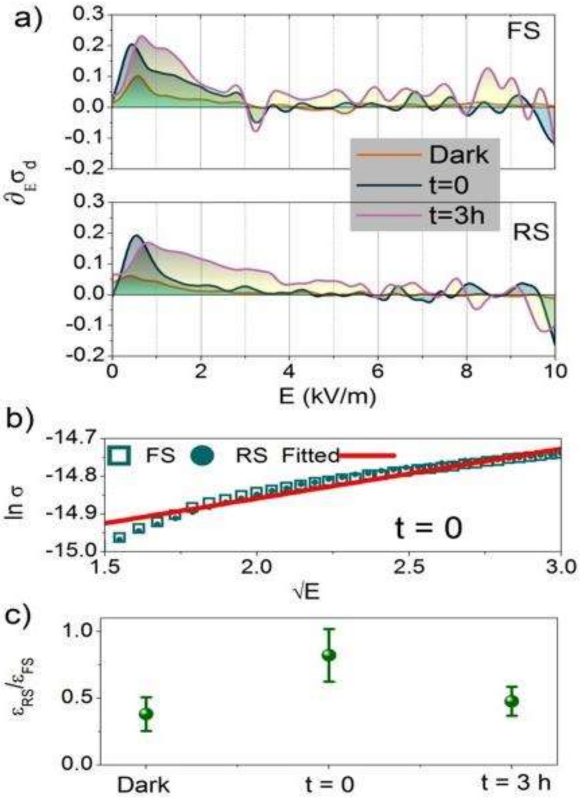

Figure 5.8: (a) Density of state ($\partial_E\sigma_d$) variation with the field and (b) the variation of a relative dielectric constant of RS with FS and (c) Frenkel–Poole fitting for just illuminated photo-current voltage variation.

The inelastic tunneling current is correlated with the energy of defect dipoles (u_{in}) spatially distributed in the sample; i.e., $J_{in} \alpha < \psi^* \mid \int u_{in}\, dx \mid \psi >$, where ψ^* and ψ represent the excited and ground state wave functions, respectively. Thus, conductivity should show the negative differential behavior. The negative differential feature can be better understood in terms of the tunneling density of state ($\partial_E\sigma_d$) variation with the field E [Fig. 5.8(a); here, σ_d is $\partial_E\sigma$]. Surprisingly, we could observe [Fig. 5.8(a)] a strong dip at the field of 3 kV/m for the FS, which is independent of illumination duration; thereafter, the oscillatory behavior is observed. This is something similar to the Gunn effect [183],[184],[185], which shows a negative value of σ_d due to the non-uniform motion of charge carriers. However, in the RS, the dip is missing, and the oscillatory behavior occurs at a higher field as compared to the FS. Thus, the Gunn effect like behavior is observed in FS and does not appear in RS in the mid-field regime for the $CsPbBr_3$ sample. The variation of superlinearity ($n = 1.1$ □ 1.5) of the J–E curve with illumination time (Fig. 5.3) suggested that the space charge limited conduction mechanism (with traps) shifts toward Frenkel– Poole from Ohmic with the continuous photoinjection. For the dark current (in the mid-field regime), the trap energy estimated using the Frenkel–Poole relation [186] ($\sigma_E = k_2\, e^{-\beta\varepsilon_{trap}}$; $k_2 = q\mu N_c\, e^{(-\frac{\beta\Delta E_{cB,vB}}{2})}$; $\varepsilon_{trap} = q(\phi_B - \sqrt{(qk_e/\varepsilon_r)E}$; $\varepsilon_r = 1.23 < \varepsilon_{r,optical} = 1.62$) is comparable with the thermal activation energy (~0.3 eV) in the grain. The Frenkel–Poole fitting at the time t = 0 for FS and RS is shown in Fig. 5.8(b). The variation of the relative dielectric constant is estimated from the slope of Frenkel–Poole fitting in FS and RS [Fig. 5.8(c)]. This suggests that the coulomb screening is always greater in FS and hence polarization. With just flooding of Sun light, photoinjection is increasing the dielectric constant in FS, while in RS, there is an increase in the dielectric constant after attaining equilibrium. Thus, hysteresis occurs due to the interplay of orientational polarization with photo- and field injection, which further depends on the field scan direction.

5.4 Conclusion

The defect centers, for example, interstitial Pb^{+2}, act as a mobile generating center, which under a combined action of photo- and space charge limited injection can capture electrons from excitons and provide a free hole for conduction. This Pb^{+2} and holes moving in the same direction with the momentum increase in the forward scan, where the possibility of carrier enhancement at the energy level of traps is possible. It results in the negative differential resistance in the forward scan. However, in the reverse scan, the momentum gets decreased, ion migration is not able to maintain its momentum, and hence, the possibility of carrier enhancement reduces. In summary, from the present study, it appears that reported mechanisms of the hysteresis, i.e., trapping–detrapping, ion migration, polarization and slow capacitive current, are interrelated. The photo-current voltage hysteresis is primarily affected by the thermionic-field emission (caused by the infrared light part of Sun light with $h\nu < E_g$), which slows down the drift velocity of hot charge carriers with field applications (forward scan) and could not affect significantly in the reverse scan. Furthermore, it would be interesting to investigate whether this drift velocity slowdown is related to domain conduction (Gunn effect) or momentum dependent splitting of spin bands (Rashba effect).

Chapter 6

Comparative Study of Perovskite and Ruddlesden Popper (RP) for Lead (Pb) and Lead-Free Halides

Publication: ***Manish Kumar***, *and Prabhakar Singh, Comparative study of Perovskite and Ruddlesden Popper for lead and lead-free halides (Under Preparation).*